

CrossMark
click for updatesCite this: *RSC Adv.*, 2016, 6, 31181

The performance and mechanism for the catalytic oxidation of dibromomethane (CH₂Br₂) over Co₃O₄/TiO₂ catalysts†

Jian Mei, Songjian Zhao, Haomiao Xu, Zan Qu and Naiqiang Yan*

Brominated hydrocarbons are a typical pollutant in exhaust gas from the synthesis process of Purified Terephthalic Acid (PTA), and may cause various environmental problems once emitted into the atmosphere. Dibromomethane (DBM) was employed as the model compound in this study, and a series of Co₃O₄/TiO₂ catalysts with various Co contents were prepared for the catalytic oxidation of DBM. The prepared catalysts were characterized by XRD, BET, SEM, TEM, XPS, H₂-TPR and NH₃-TPD. Among the prepared catalysts, CoTi-5 (5 wt% Co/TiO₂) showed the highest catalytic activity, with T₉₀ at about 346 °C, which was mainly attributed to the enrichment of well-dispersed Co₃O₄ and the high surface Co³⁺/Co²⁺ ratio, as it could provide more surface active sites and active oxygen species. The kinetic study showed that the reaction order of DBM was pseudo first-order and the reaction order of oxygen was approximately zero-order. A plausible DBM reaction mechanism over Co₃O₄/TiO₂ catalysts was also proposed based on the results of *in situ* FTIR and the analysis of gas products by GC-MS. The reaction process started with the adsorption on surface oxygen vacancies, breakage of C–Br bonds and partial dissociation of C–H bonds with the formation of intermediate species, and then the intermediate species were further oxidized to form CO and CO₂.

Received 6th January 2016

Accepted 15th March 2016

DOI: 10.1039/c6ra00372a

www.rsc.org/advances

1. Introduction

In recent years, China has become the largest producer and consumer of Purified Terephthalic Acid (PTA) in the world. With the expansion of the PTA production scale, concerns have been raised about atmospheric emission from PTA exhaust gas,¹ and protests against such projects by several large groups have taken place in China in the past years. Typically, the untreated PTA exhaust gas is a mixture of various organic components, including carbon monoxide, acetic acid methyl ester, *p*-xylene (PX) and brominated hydrocarbon, which can cause great threats to the environment and human health once emitted.² Up to now, the treatment methods of PTA exhaust gas mainly include activated carbon adsorption, the thermal oxidation method and catalytic oxidation. Catalytic oxidation is considered to be the most promising technology for removal of PTA exhaust gas due to its low consumption of energy, high efficiency and its excellent selectivity towards the formation of the less harmless products.³ However, the presence of brominated hydrocarbon easily causes the catalysts bromine poisoning, and then the catalysts become deactivation. Thus, the key issue of

this technology is the available of high activity and high stability catalysts on the removal of brominated hydrocarbon.

At present, various catalytic materials have been used as catalysts for the catalytic oxidation of brominated hydrocarbon, including noble metal and transition metal oxide catalysts.^{4,5} Although noble metal catalysts exhibit excellent activities, the high cost and low thermal stability restrain their wide applications on industries. Hence, further efforts are demanded to develop the cheap catalysts with high activity and high stability. As a typical transition metal oxide, cobalt oxides have been widely studied for low temperature catalytic oxidation. For example, Rivas *et al.*⁶ studied the different synthesis routes of nanocrystalline Co₃O₄, and found that the nanocrystalline Co₃O₄ prepared by precipitation method decomposed 1,2-dichloroethane at the lowest temperature, no appreciable deactivation with time on stream. As a halogenated hydrocarbon, brominated hydrocarbon may be similar to chlorinated hydrocarbon in the certain properties. Therefore, Co₃O₄ may be a good candidate for the catalytic oxidation of brominated hydrocarbon.

In this study, dibromomethane (DBM) chosen as a model brominated hydrocarbon was evaluated in a fixed-bed flow reactor. A series of Co₃O₄/TiO₂ catalysts with various Co contents were prepared by a conventional impregnation method. The physical and chemical properties of the catalysts, as well as DBM conversion, were investigated. The product distribution and catalyst stability were studied, and kinetic parameters of DBM oxidation reaction were also calculated.

School of Environmental Science and Engineering, Shanghai Jiao Tong University, 800 Dong Chuan Road, Shanghai, 200240, PR China. E-mail: nqyan@sjtu.edu.cn; Fax: +86 21 54745591; Tel: +86 21 54745591

† Electronic supplementary information (ESI) available. See DOI: 10.1039/c6ra00372a

Furthermore, based on the results of *in situ* FTIR and the analysis of gas products by GC-MS, a plausible DBM reaction mechanism over $\text{Co}_3\text{O}_4/\text{TiO}_2$ catalysts was proposed.

2. Experimental section

2.1 Catalyst preparation

A series of $\text{Co}_3\text{O}_4/\text{TiO}_2$ catalysts with various Co contents (1, 2.5, 5, 10 and 25 wt%, calculated by the weight percentage of Co/ TiO_2) were prepared by a conventional impregnation method. Commercial P25 TiO_2 (Degussa; 80% anatase and 20% rutile phases) was used as a support. In a typical preparation, $\text{Co}(\text{NO}_3)_3 \cdot 6\text{H}_2\text{O}$ used as the Co_3O_4 precursor was dissolved in ultrapure water, then P25 TiO_2 was added into $\text{Co}(\text{NO}_3)_3 \cdot 6\text{H}_2\text{O}$ solution and stirred for 4 h. All the water was evaporated using a rotary evaporation apparatus. The obtained powders were dried at 60 °C overnight and calcined in air at 500 °C for 3 h. The samples were marked for CoTi-1, CoTi-2.5, CoTi-5, CoTi-10 and CoTi-25, respectively.

2.2 Catalyst characterization

The X-ray diffraction (XRD) measurements were recorded on a Shimadzu XRD-6100, and the data were collected in the 2θ range 10–80 ° with a scanning velocity of 10° min^{-1} . The BET (Brunauer–Emmett–Teller) surface areas of the samples were determined using N_2 adsorption at –196 °C and using a quartz tube (Quantachrome 2200e). The morphology and microstructure of the samples were analyzed by scanning electron microscope (SEM) (JSM-7800F) and transmission electron microscopy (TEM) (JEOL-2100F). The samples were dispersed in ethanol with strong sonication before analysis. The H_2 -TPR experiments were investigated on the chemisorption analyzer (2920, AutoChem II, Micromeritics). Prior to the measurement, the samples were pretreated in Ar stream at 300 °C for 2 h. After cooling down to 50 °C, the samples were heated to 1000 °C with temperature ramp of 10 °C min^{-1} in 10% H_2/Ar . The NH_3 -TPD experiments were also investigated on the chemisorption analyzer (2920, AutoChem II, Micromeritics). Prior to the measurement, the 200 mg samples were pretreated in He stream at 400 °C for 2 h. Then NH_3 adsorption was performed at 50 °C with 10% NH_3/He for 1 h. Next, the samples were purged in He stream for 30 min to remove physically adsorbed NH_3 , and then heated to 600 °C with temperature ramp of 10 °C min^{-1} with a 50 mL min^{-1} He flow. The X-ray photoelectron spectroscopy (XPS) results were recorded with an AXIS Ultra DLD (Shimadzu-Kratos) spectrometer with Al K α as the excitation source, and the C 1s line at 284.8 eV was used as a reference for the binding energy calibration.

2.3 Catalytic activity evaluation

The performances of the catalysts for DBM oxidation were tested in a fixed-bed quartz tube reactor (i.d 6 mm) containing 130 mg catalyst. The typical reactant gas stream was composed of 500 ppm DBM, 10% O_2 and N_2 as the balance gas in 150 mL min^{-1} , corresponding to a gas hourly space velocity (GHSV) of 60 000 h^{-1} . The reaction was run from 150 to 450 °C in a step

mode with a 20 min plateau at each temperature investigated. The inlet and outlet gases were analyzed by a gas chromatograph equipped with a flame ionization detector. The removal efficiency of DBM was defined as:

$$\eta = \frac{C_0 - C}{C_0} \times 100\% \quad (1)$$

where C_0 and C were the inlet and outlet DBM concentrations, respectively. The gas products were detected by gas chromatography and mass spectrometry (GCMS-QP2010, Shimadzu). The final products CO and CO_2 were measured using a gas chromatograph (GC-14B, Shimadzu) equipped with a FID detector with methane conversion oven. Br_2 and HBr were absorbed in a KI solution firstly. Then, Br_2 concentration was determined by the titration with sodium thiosulfate using starch solution as an indicator. The concentration of bromide ions in the bubbled solution was determined by using an ion chromatography. The selectivity of CO, CO_2 , Br_2 and HBr was defined as, respectively:

$$S_{\text{CO}} = \frac{[\text{CO}]}{[C_T]} \times 100\% \quad (2)$$

$$S_{\text{CO}_2} = \frac{[\text{CO}_2]}{[C_T]} \times 100\% \quad (3)$$

$$S_{\text{Br}_2} = \frac{[\text{Br}_2]}{[C_{\text{Br}}]} \times 100\% \quad (4)$$

$$S_{\text{HBr}} = \frac{[\text{HBr}]}{[C_{\text{Br}}]} \times 100\% \quad (5)$$

where $[\text{CO}]$ and $[\text{CO}_2]$ were the amount of CO and CO_2 (ppm) after the reaction, $[C_T]$ was the amount of carbon atom (ppm) in oxidized DBM during the reaction, which could be calculated by eqn (6):

$$[C_T] = ([\text{CH}_2\text{Br}_2]_0 - [\text{CH}_2\text{Br}_2]) \quad (6)$$

where $[\text{CH}_2\text{Br}_2]_0$ and $[\text{CH}_2\text{Br}_2]$ were the amount of DBM (ppm) in the gas stream before and after the reaction, respectively. $[\text{Br}_2]$ and $[\text{HBr}]$ were the amount of Br_2 and HBr (ppm) after the reaction, $[C_{\text{Br}}]$ was the amount of bromine atom (ppm) in oxidized DBM during the reaction, which could be calculated by eqn (7):

$$[C_{\text{Br}}] = ([\text{CH}_2\text{Br}_2]_0 - [\text{CH}_2\text{Br}_2]) \times 2 \quad (7)$$

2.4 Kinetic study

The external diffusion effect was investigated by varying the speed of feed gas while keeping a constant GHSV (60 000 h^{-1}). Similarly, the internal diffusion effect was checked by changing the particle size of the catalysts (as shown in Fig. S2†). The results showed that the catalytic reaction was operated without diffusional limitation below 10% conversion of DBM. The kinetic experiments were carried out under differential

condition (the maximum conversion was controlled below 10%). And the reaction rate was calculated as follows:

$$-r = F \times \frac{dx}{dW} \approx F \times \frac{x}{W} \quad (8)$$

where $-r$ ($\text{mol g}^{-1} \text{s}^{-1}$) was the reaction rate, F (mol s^{-1}) was the inlet flow rate, x (%) was the conversion of DBM, and W was the catalyst weight (g).

2.5 In situ FTIR experiments

In situ FTIR spectra were recorded on a Fourier transform infrared spectrometer (FTIR, Nicolet 6700) equipped with a smart collector and an MCT detector cooled by liquid N_2 . The diffuse reflectance FTIR measurements were carried out in a high-temperature cell with ZnSe windows. Mass flow controllers and a sample temperature controller were used to simulate the real reaction conditions. *In situ* FTIR spectra were recorded by accumulating 100 scans at a resolution of 4 cm^{-1} . Prior to each experiment, all the samples were pretreated with 10% O_2/N_2 at 400°C for 2 h. Spectra of the clean catalyst surface were collected and used as the background at different temperature. Then, a 500 ppm DBM/10% O_2/N_2 stream was introduced into the IR cell at 50°C for 1 h. Subsequently, the catalyst was treated in flowing 10% O_2/N_2 at different temperature. *In situ* FTIR spectra were collected at different temperature where a steady was reached.

3. Results and discussion

3.1 Catalytic performance for DBM oxidation

Fig. 1 shows the activity of $\text{Co}_3\text{O}_4/\text{TiO}_2$ catalysts for DBM oxidation as a function of temperature. It is convenient to compare the catalytic activities of these catalysts by using the reaction temperatures T_{50} and T_{90} (corresponding to the DBM conversion = 50 and 90%). The results indicated that the conversion of DBM decreased in the following order, $\text{CoTi-5} >$

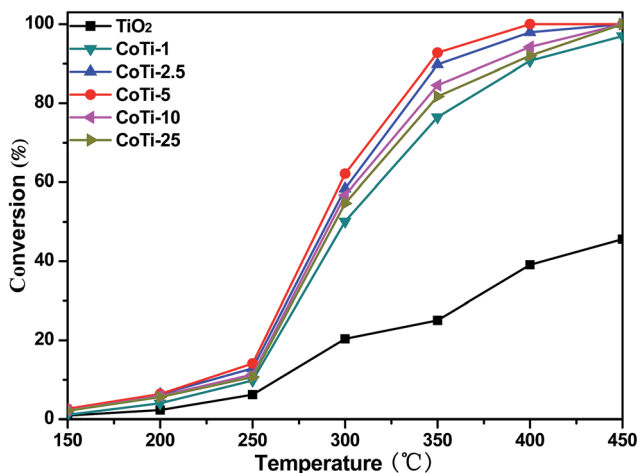


Fig. 1 DBM conversion over $\text{Co}_3\text{O}_4/\text{TiO}_2$ catalysts with various Co contents; gas composition: 500 ppm DBM, 10% O_2 and N_2 balance; GHSV = $60\,000 \text{ h}^{-1}$.

$\text{CoTi-2.5} > \text{CoTi-10} > \text{CoTi-25} > \text{CoTi-1} > \text{TiO}_2$. Pure TiO_2 exhibited the lowest activity with $T_{50} > 450^\circ\text{C}$. However, with the presence of Co_3O_4 species on TiO_2 , the activities of catalysts were remarkably improved and the conversion curves shifted into lower temperature. Moreover, it was found that $\text{Co}_3\text{O}_4/\text{TiO}_2$ catalysts exhibited a rising conversion with the increase of Co content from 0% to 5%. CoTi-5 showed the highest activity, and the T_{90} value was about 346°C . However, further increasing the Co content to 25%, $\text{Co}_3\text{O}_4/\text{TiO}_2$ catalysts showed a declined catalytic activity. This result revealed that there were not enough active sites on the surface of the catalyst when the Co content was below 5%, and the catalytic activity dropped. Nevertheless, when the Co content was above 5%, the Co_3O_4 particles dispersed on the surface began to agglomerate, and the Co_3O_4 particles on the surface overlapped and the number of active sites was reduced, which decreased the catalytic activity.

3.2 Catalyst characterization

Fig. 2 shows the XRD patterns of $\text{Co}_3\text{O}_4/\text{TiO}_2$ catalysts. For all the catalysts, the pure Co phase identified was spinel-structured Co_3O_4 (PDF#43-1003). The other observed diffraction peaks were attributed to TiO_2 , which were in the form of anatase and rutile. No representative diffraction peaks of Co_3O_4 were observed when Co content was less than 5%. The Co_3O_4 crystalline might be formed in CoTi-5 and some small characteristic peaks were observed, which might be due to its small size or well dispersed state.⁷ Only when the Co content exceeded 10%, the remarkable XRD peaks representing Co_3O_4 could be observed in the patterns and increasing Co content enhanced the intensity of the diffraction peaks of the spinel-structured Co_3O_4 .

Table 1 displays the specific surface area, pore volume and pore diameter of $\text{Co}_3\text{O}_4/\text{TiO}_2$ catalysts. After the loading of Co into TiO_2 , the specific surface area began to decrease, owing to a clogging or covering of the TiO_2 support. Moreover, when the Co content increased from 1 to 5%, the specific surface area gradually increased. However, with further increasing the Co

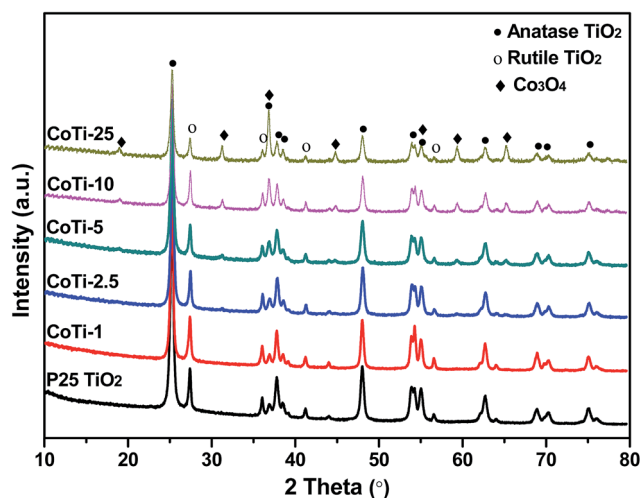


Fig. 2 XRD patterns of $\text{Co}_3\text{O}_4/\text{TiO}_2$ catalysts with various Co contents.

Table 1 Specific surface area, pore volume and pore diameter of $\text{Co}_3\text{O}_4/\text{TiO}_2$ catalysts

Samples	Specific surface area ($\text{m}^2 \text{g}^{-1}$)	Pore volume ($\text{cm}^3 \text{g}^{-1}$)	Pore diameter (nm)
TiO_2	53.233	0.13	23.277
CoTi-1	34.635	0.304	25.34
CoTi-2.5	36.999	0.314	24.516
CoTi-5	40.32	0.362	24.785
CoTi-10	32.433	0.275	24.871
CoTi-25	29.473	0.202	23.277

content to 25%, the specific surface area began to decrease. CoTi-5 had the biggest specific surface area among all the $\text{Co}_3\text{O}_4/\text{TiO}_2$ catalysts, and it might have more active sites for catalytic reaction.

To obtain the microscopic morphology information of the catalysts, transmission electron microscope (TEM) analysis of

$\text{Co}_3\text{O}_4/\text{TiO}_2$ catalysts was performed. As shown in Fig. 3, the TEM images in Fig. 3(a–e) exhibited evenly distributed $\text{Co}_3\text{O}_4/\text{TiO}_2$ nanoparticles with diameters of 30–40 nm. The high-resolution transmission electron microscopy (HRTEM) image of CoTi-25 (Fig. 3(f)) further confirmed the crystalline structure of $\text{Co}_3\text{O}_4/\text{TiO}_2$. As seen from the figure, the interplanar spacing of 0.28 nm and 0.35 nm corresponded to Co_3O_4 (220) and TiO_2 (101),^{8,9} respectively, indicating that cobalt was loaded on the surface of TiO_2 and existed in the form of Co_3O_4 , consistent with the XRD results.

XPS is a good tool to investigate the surface element composition, element oxidation state, and adsorbed species of a material.¹⁰ Fig. 4 shows the Co 2p and O 1s spectra of $\text{Co}_3\text{O}_4/\text{TiO}_2$ catalysts. As shown in Fig. 4(a), for all the $\text{Co}_3\text{O}_4/\text{TiO}_2$ catalysts with various Co contents, there were two main peaks corresponding to Co 2p_{3/2} and Co 2p_{1/2} at 779.9–781.3 and 795.1–797.2 eV, respectively, with satellite peaks. By performing peak-fitting deconvolution, the main Co 2p_{3/2} peak could be separated into two peaks, the lower binding energy was belong

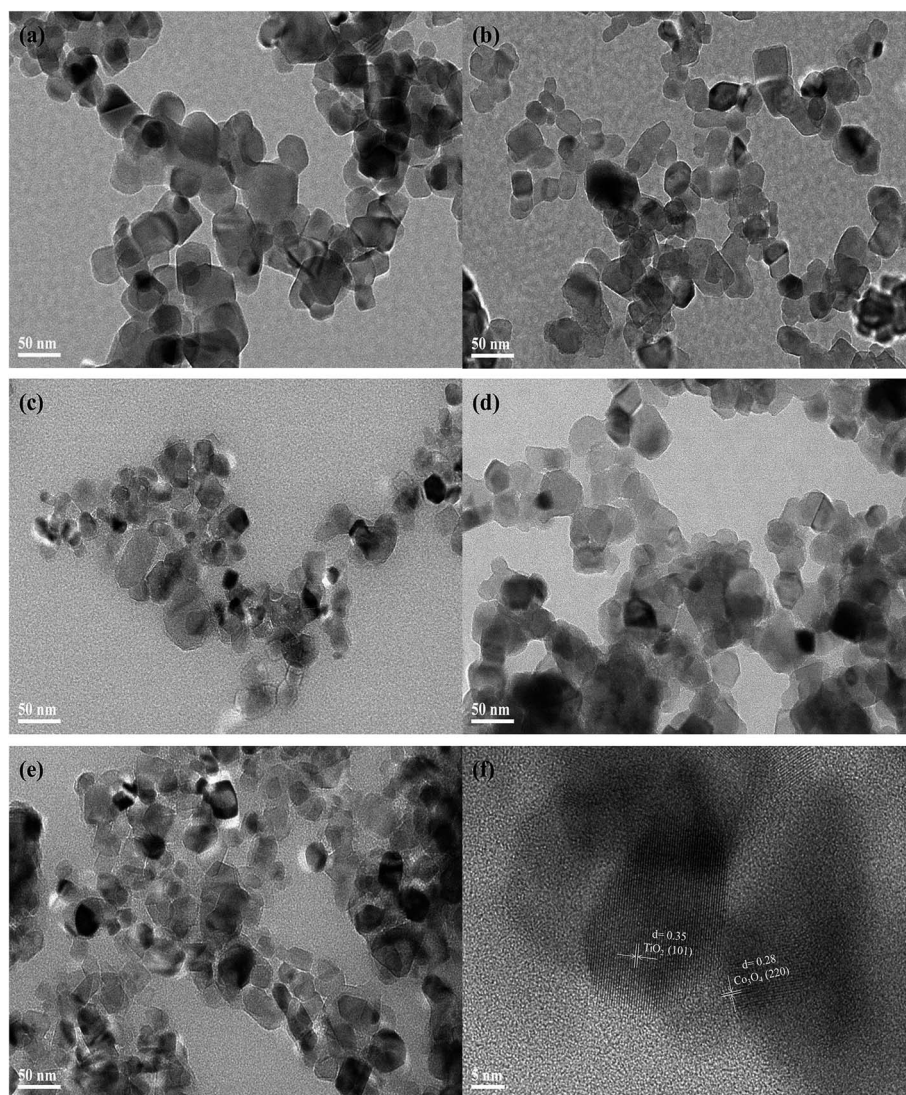


Fig. 3 TEM images of (a) CoTi-1, (b) CoTi-2.5, (c) CoTi-5, (d) CoTi-10 and (e) CoTi-25 and HRTEM image of (f) CoTi-25.

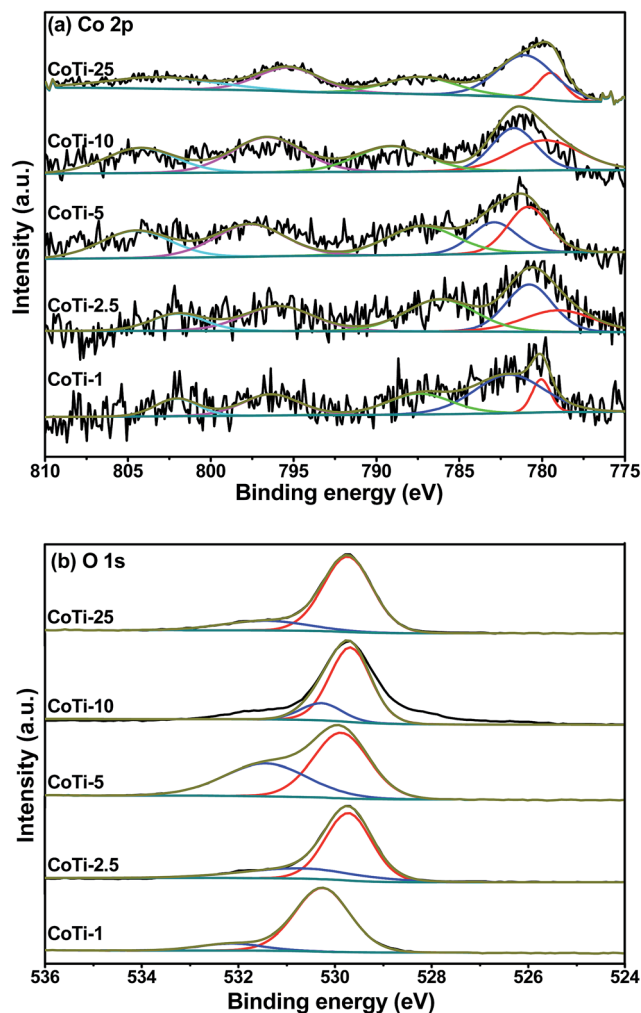


Fig. 4 XPS spectra of (a) Co 2p and (b) O 1s for $\text{Co}_3\text{O}_4/\text{TiO}_2$ catalysts with various Co contents.

to Co^{3+} , while the higher binding energy could be ascribed to Co^{2+} .¹¹ A spectral feature that could distinguish between Co^{2+} and Co^{3+} was a satellite for Co^{2+} peak, because photoemitted electrons interacted with core vacancies and valence electrons of Co^{2+} but not with those of Co^{3+} .¹² As shown in Table 2, the surface $\text{Co}^{3+}/\text{Co}^{2+}$ ratio increased from 0.23 to 1.23 as Co content from 1 to 5%, indicating an increase of Co^{3+} percentage on the catalyst surface. However, the surface $\text{Co}^{3+}/\text{Co}^{2+}$ ratio decreased as further increasing Co content, which illustrated that excessive Co_3O_4 loading decreased the surface $\text{Co}^{3+}/\text{Co}^{2+}$ ratio. The cation distribution of the spinel-structured Co_3O_4

Table 2 XPS parameters of $\text{Co}_3\text{O}_4/\text{TiO}_2$ catalysts

Samples	$\text{Co}^{3+}/\text{Co}^{2+}$	$\text{O}_{\text{ads}}/\text{O}_{\text{lat}}$
CoTi-1	0.23	0.13
CoTi-2.5	0.69	0.38
CoTi-5	1.32	0.76
CoTi-10	1.11	0.23
CoTi-25	0.30	0.22

had been demonstrated to be $\text{Co}^{2+}[\text{Co}^{3+}]_2\text{O}_4$, and the more surface $\text{Co}^{3+}/\text{Co}^{2+}$ ratio could lead to more anionic defects. This had been shown to bring excess surface oxygen and promote gas molecular adsorption.¹³

As shown in Fig. 4(b), one can see an asymmetrical O 1s XPS peak of the catalysts that could be resolved into two components at BE = 529.7–530.3 and 530.4–532.1 eV. The former was due to the surface lattice oxygen (O_{lat}), whereas the latter was due to the surface adsorbed oxygen (O_{ads}).^{14–16} It was also found from Table 2 that the surface $\text{O}_{\text{ads}}/\text{O}_{\text{lat}}$ ratio decreased in the order of $\text{CoTi-5} > \text{CoTi-2.5} > \text{CoTi-10} > \text{CoTi-25} > \text{CoTi-1}$. The formation of oxygen adsorbed species was due to the presence of surface oxygen vacancies on $\text{Co}_3\text{O}_4/\text{TiO}_2$ catalysts, which implied that there might be the coexistence of Co^{3+} and Co^{2+} ions on $\text{Co}_3\text{O}_4/\text{TiO}_2$ catalysts. Such a deduction was supported by the Co $2p_{3/2}$ XPS results of the catalysts. In general, surface adsorbed oxygen is more active than lattice oxygen due to its high mobility, and it plays an important role in catalytic oxidation reaction.¹¹ Hence, more surface adsorbed oxygen will lead to the stronger oxidization ability, which is consistent with our DBM oxidation results.

Fig. 5 shows the H_2 -TPR profiles of $\text{Co}_3\text{O}_4/\text{TiO}_2$ catalysts. As shown in the figure, the H_2 -TPR profiles of CoTi-1, CoTi-10 and CoTi-25 exhibited two reduction peaks, which were related to the reduction of Co^{3+} to Co^{2+} at lower temperature and Co^{2+} to Co^0 at higher temperature, respectively.⁷ Whereas the H_2 -TPR profiles of CoTi-2.5 and CoTi-5 exhibited three reduction peaks between 300 °C and 500 °C, the first peak was attributed to the reduction process of some surface oxygen, and the second and third peaks were attributed to the reduction of Co^{3+} to Co^{2+} and Co^{2+} to Co^0 , respectively.¹⁷ It could also be observed that these reduction peaks shifted to lower temperature with an increase in the Co content. The peak at 434 °C in CoTi-1 could be related to the reduction peak of isolated Co, and the peak at 640 °C could be attributed to the strong interaction between Co and Ti.¹⁸ When Co content was higher than 2.5%, two reduction peaks appeared at about 419 °C and

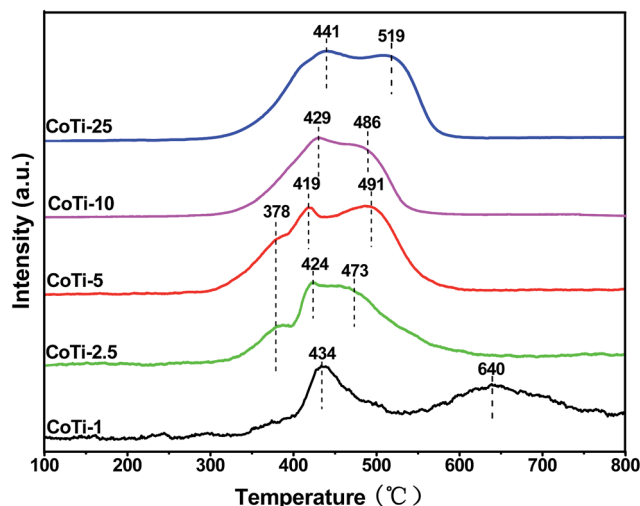


Fig. 5 H_2 -TPR profiles of $\text{Co}_3\text{O}_4/\text{TiO}_2$ catalysts with various Co contents.

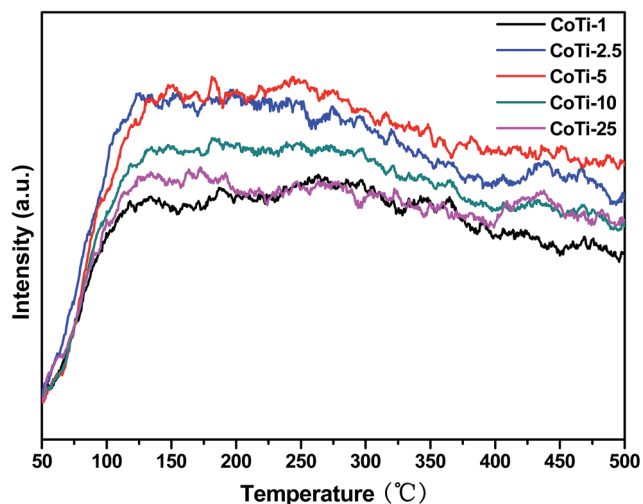


Fig. 6 NH_3 -TPD profiles of $\text{Co}_3\text{O}_4/\text{TiO}_2$ catalysts with various Co contents.

Table 3 Products in outlet at each evaluated temperature over CoTi-5

Temperature (°C)	Detected substances
150	CH_2Br_2 , CH_3Br , CO , HBr , H_2O
200	CH_2Br_2 , CH_3Br , CO , CO_2 , HBr , H_2O
250	CH_2Br_2 , CO , CO_2 , HBr , H_2O
300	CH_2Br_2 , CO , CO_2 , HBr , H_2O
350	CH_2Br_2 , CO , CO_2 , HBr , Br_2 , H_2O
400	CO , CO_2 , HBr , Br_2 , H_2O
450	CO , CO_2 , HBr , Br_2 , H_2O

491 °C were observed, which could be assigned to Co_3O_4 crystalline. As further increasing the Co content, these reduction peaks slightly shifted to higher temperature, which might be due to the sintering.¹⁹ CoTi-5 showed the best reducibility, which probably resulted in its high catalytic performance for DBM oxidation.

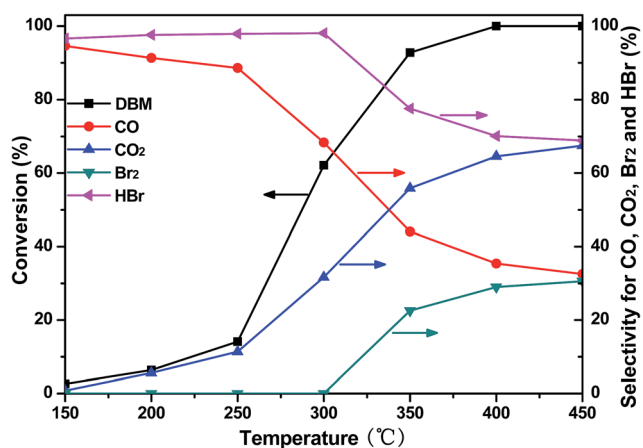


Fig. 7 DBM conversion and selectivity for CO , CO_2 , Br_2 and HBr as a function of temperature over CoTi-5.

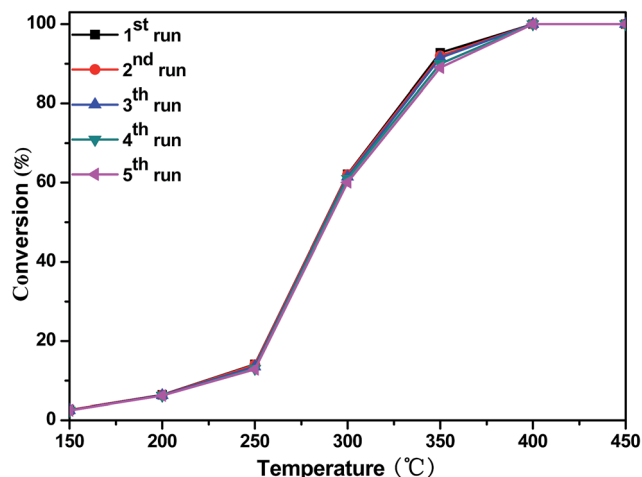


Fig. 8 DBM conversion as a function of temperature over CoTi-5 for first to fifth run ($\text{GHSV} = 60\,000\ \text{h}^{-1}$).

Surface acidities of the catalysts are found to have significantly influence on VOCs oxidation as they provide sites for the chemisorption of VOCs molecules.²⁰ Therefore, surface acidities

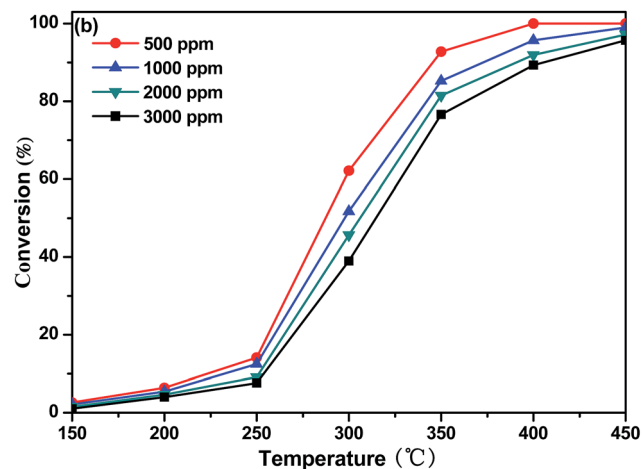
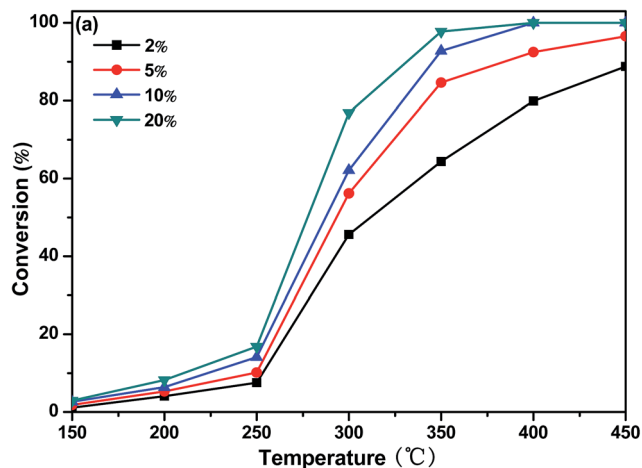


Fig. 9 DBM conversion as a function of temperature over CoTi-5 in various (a) O_2 and (b) DBM concentrations ($\text{GHSV} = 60\,000\ \text{h}^{-1}$).

of the catalysts are measured by NH_3 -TPD, and the results are shown in Fig. 6. For all the $\text{Co}_3\text{O}_4/\text{TiO}_2$ catalysts, a broad shoulder peak appeared in the range of 120 °C and 150 °C, which could be the weak acid sites. Moreover, the amount of the acid sites decreased in order of $\text{CoTi-5} > \text{CoTi-2.5} > \text{CoTi-10} > \text{CoTi-25} > \text{CoTi-1}$. CoTi-5 had the most acid sites, which could be beneficial for the catalytic oxidation of DBM.

3.3 Analysis of products

It should be noticed that for brominated hydrocarbon oxidation, high conversion is not the only criterion for good catalysts, and selectivity of the products is more important. The ideal decomposition products of brominated hydrocarbon are CO_2 and HBr or Br_2 . Thus, the products in outlet at each evaluated temperature over CoTi-5 were analyzed by GC-MS and the results were listed in Table 3. As seen in Table 3, the byproduct CH_3Br was emerged at low temperature (below 200 °C) and it was disappeared with the increase of temperature. CO , HBr and H_2O were always existed at each evaluated temperature, CO_2 was generated above 200 °C and Br_2 was generated above 350 °C. Up to 400 °C, CH_2Br_2 was completely disappeared.

Fig. 7 shows the DBM conversion and selectivity for CO , CO_2 , Br_2 and HBr as a function of temperature over CoTi-5. As can be

seen, the main products of DBM conversion were CO , CO_2 and HBr at a low temperature range (below 300 °C). However, with the increase of temperature, the amount of CO_2 was gradually improved and its selectivity was exceeded 50% at 335 °C due to the further oxidation of CO . When the temperature was above 350 °C, Br_2 was generated, which might be attributed to the Deacon reaction ($4\text{HBr} + \text{O}_2 = 2\text{Br}_2 + 2\text{H}_2\text{O}$).²¹ With the further increase of temperature, the selectivity for Br_2 was also further improved, and its selectivity got to 31% at 450 °C. Therefore, the main products of DBM conversion were CO , CO_2 , HBr and Br_2 at a high temperature range (above 350 °C). However, the deep oxidation (the oxidation of CO to CO_2) still needed to be further improved.

3.4 Catalyst stability

For commercial application, the stability of the catalyst is an important factor. The stability of the catalyst in the reaction was tested by reusing the catalyst in consecutive oxidation cycles and by performing long catalytic runs at constant oxidation temperature. As shown in Fig. 8, CoTi-5 was submitted to successive oxidation cycles. In this case, CoTi-5 also maintained its catalytic activity well after five oxidation cycles. The evolution of DBM conversion with time on stream at 300 °C over CoTi-5 is

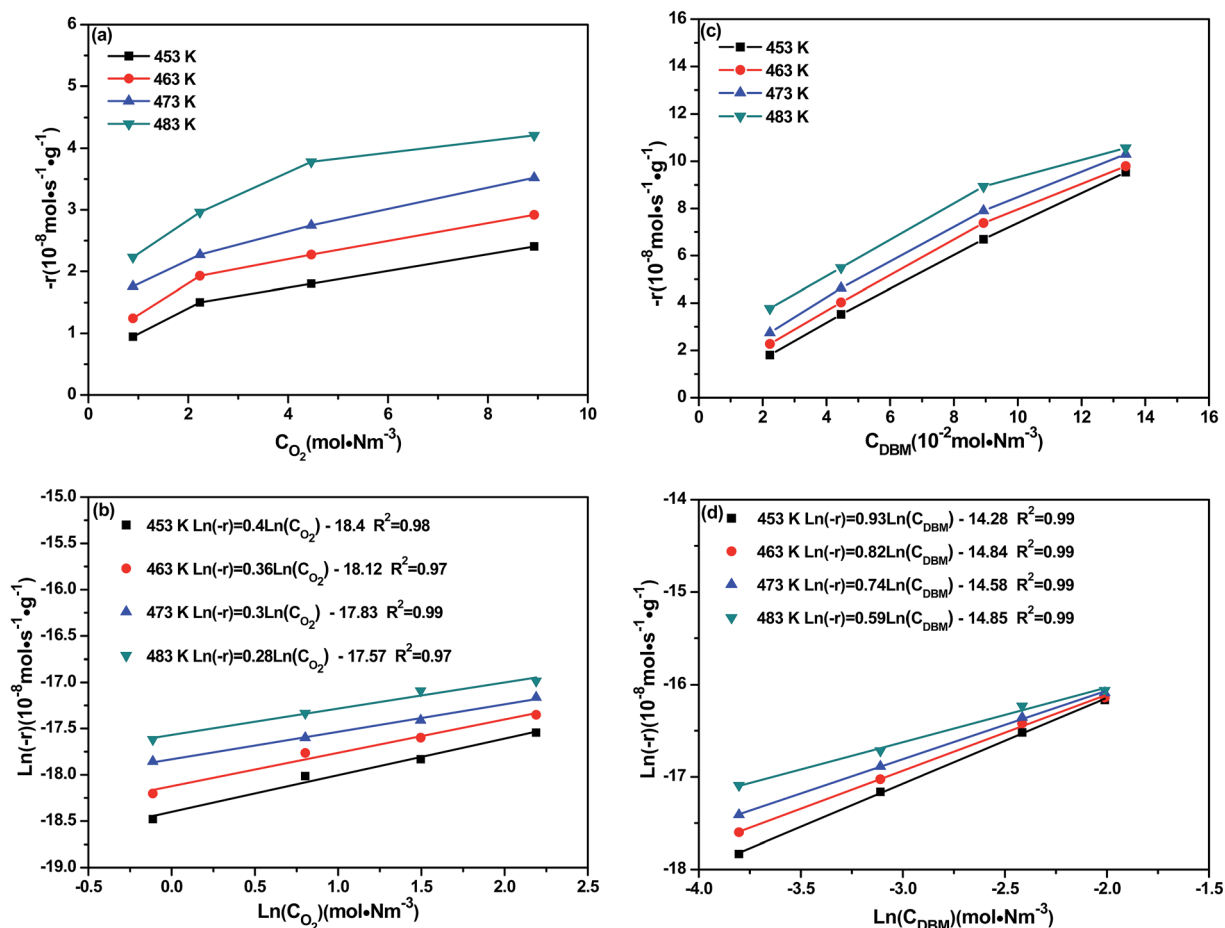


Fig. 10 Dependence of the DBM reaction rate on the (a and b) oxygen partial pressure and (c and d) DBM partial pressure over CoTi-5.

presented in Fig. S3.† CoTi-5 could maintain its catalytic activity well after 600 min of reaction. These results showed that CoTi-5 had a good stability for DBM oxidation.

3.5 Kinetic study

Fig. 9 shows DBM conversion as a function of temperature over CoTi-5 under various oxygen and inlet DBM concentrations. As shown in Fig. 9(a), the conversion of DBM increased with the increase of oxygen concentration, and the observed T_{50} changed from 313 °C to 278 °C (corresponding to the oxygen concentrations of 2% and 20%, respectively). In Fig. 9(b), it was found that the conversion of DBM decreased with the increase of DBM concentration. Observed T_{50} changed from 287 °C to 314 °C (corresponding to the DBM concentrations of 500 ppm and 3000 ppm, respectively). These data illustrated that both the oxygen and the DBM concentrations might be not very sensitive parameters. To gain further insight in this question, kinetic studies were carried out by investigating the effect of oxygen and inlet DBM concentrations on the reaction rate ($-r$) as shown in Fig. 10. The conversions were controlled below 10% to obtain initial reaction rate for all conditions. It was found that all the data could be explained by the power law equation as follows:

$$-r = k C_{O_2}^m C_{DBM}^n \quad (9)$$

where k was the kinetic constant, C_{O_2} (mol N m^{-3}) was the O_2 concentration, C_{DBM} (mol N m^{-3}) was the inlet DBM concentration, m and n were the apparent reaction orders of oxygen and DBM, respectively. The values of m and n were obtained from the slope of each line in Fig. 10(b) and (d).

As shown in Fig. 10(a), the reaction rate grew nonlinearly with the increase of oxygen concentration in the studied temperature range. In Fig. 10(c), a similar tendency could also be seen, but the growth of the reaction rate seemed to be more rapidly with the increase of DBM concentration. Really, compared with the values of n , the values of m were lower (shown in Table 4). Particularly, the reaction order of DBM was pseudo first-order, which indicated that the adsorption of DBM on the catalyst surface was difficult. However, strong adsorption caused apparent zero-order for reaction, because all the active sites on the catalyst surface were occupied. For oxygen as a reactant, the reaction order was closed to zero-order. It could be supposed that if the intermediates could directly react with gas-phase oxygen, the reaction order of oxygen would be approximate first-order, thus indicating that DBM molecular might not directly react with gas-phase oxygen. Moreover, on the basis of Arrhenius equation, the apparent activation energy (E_a) was also obtained.

Table 4 Kinetic parameters for DBM oxidation over CoTi-5

Kinetic parameter	453 K	463 K	473 K	483 K
m	0.4	0.36	0.3	0.28
n	0.93	0.82	0.74	0.59
E_a (kJ mol^{-1})	23.4			

3.6 In situ FTIR experiments

The kinetic results showed an important feature of the catalytic reaction, which was the apparent reaction order of oxygen or DBM was between zero- and first-order. However, kinetic method tended to be a general method, which still could not explain the reaction mechanism directly. For example, the understanding in regard to intermediate products of the catalytic reaction needed more direct tools. Hence, the *in situ* FTIR method was used to study the mechanism on the interaction between DBM molecule and $\text{Co}_3\text{O}_4/\text{TiO}_2$ catalysts.

In situ FTIR spectra collected at different temperature over CoTi-5 are shown in Fig. 11(a) and (b). After exposed to the mixture of 500 ppm DBM, 10% O_2 and N_2 balance, the bands at 3072, 2992, 1600 and 1201 cm^{-1} were observed. The bands at 3072, 2992 and 1201 cm^{-1} were attributed to antisymmetric

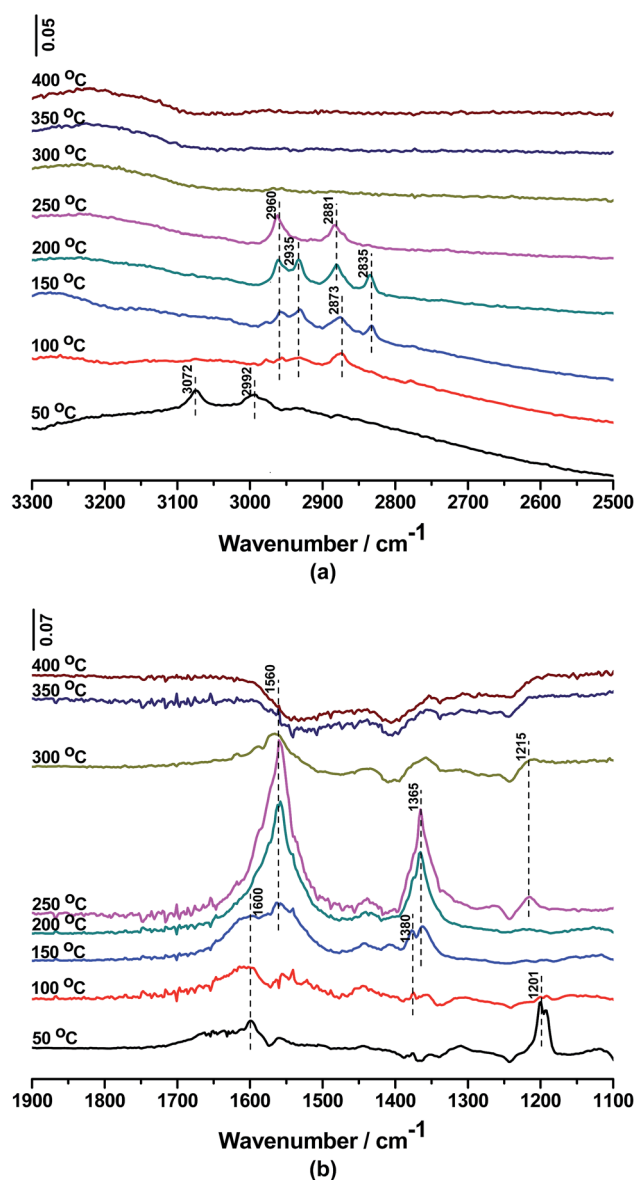


Fig. 11 *In situ* FTIR spectra of DBM oxidation over CoTi-5 (a, b) as a function of temperature.

the reaction order of DBM was pseudo first-order and the reaction order of oxygen was approximate zero-order over CoTi-5, respectively. Thirdly, some reaction intermediates such as formate species and methoxy species were detected by *in situ* FTIR, based on which a plausible DBM reaction mechanism over Co₃O₄/TiO₂ catalysts was proposed. The reaction process started with the adsorption on surface oxygen vacancies, breakage of C–Br bonds and partial dissociation of C–H bonds with the formation of intermediate species, and then the further dissociation of C–H bonds and the oxidation of CO to CO₂ were started, and finally the reaction recycle was finished.

Acknowledgements

This work was supported by the Major State Basic Research Development Program of China (973 Program, No. 2013CB430005).

References

- 1 B. Chen, J. Carson, J. Gibson, R. Renneke, T. Tacke, M. Reisinger, R. Hausmann, A. Geisselmann, G. Stochniol and P. Panster, *Chemical Industries*, Marcel Dekker, New York, 2003, pp. 179–190.
- 2 M. Moreton, *Int. J. Hydrocarbon Eng.*, 1998, **3**, 57–58.
- 3 T. Cai, H. Huang, W. Deng, Q. Dai, W. Liu and X. Wang, *Appl. Catal., B*, 2015, **166–167**, 393–405.
- 4 K. Ding, A. R. Derk, A. Zhang, Z. Hu, P. Stoimenov, G. D. Stucky, H. Metiu and E. W. McFarland, *ACS Catal.*, 2012, **2**, 479–486.
- 5 G. R. Lester, *Catal. Today*, 1999, **53**, 407–418.
- 6 B. de Rivas, R. López-Fonseca, C. Jiménez-González and J. I. Gutiérrez-Ortiz, *J. Catal.*, 2011, **281**, 88–97.
- 7 Y. Liu, Y. Wang, H. Wang and Z. Wu, *Catal. Commun.*, 2011, **12**, 1291–1294.
- 8 L. Hu, Q. Peng and Y. Li, *J. Am. Chem. Soc.*, 2008, **130**, 16136–16137.
- 9 S. Zhao, Z. Li, Z. Qu, N. Yan, W. Huang, W. Chen and H. Xu, *Fuel*, 2015, **158**, 891–897.
- 10 F. Wang, H. Dai, J. Deng, G. Bai, K. Ji and Y. Liu, *Environ. Sci. Technol.*, 2012, **46**, 4034–4041.
- 11 H. Hu, S. Cai, H. Li, L. Huang, L. Shi and D. Zhang, *ACS Catal.*, 2015, **5**, 6069–6077.
- 12 T. Chuang, C. Brundle and D. Rice, *Surf. Sci.*, 1976, **59**, 413–429.
- 13 B. Meng, Z. Zhao, X. Wang, J. Liang and J. Qiu, *Appl. Catal., B*, 2013, **129**, 491–500.
- 14 A. Carley, M. Roberts and A. Santra, *J. Phys. Chem. B*, 1997, **101**, 9978–9983.
- 15 N. Yamazoe, Y. Teraoka and T. Seiyama, *Chem. Lett.*, 1981, 1767–1770.
- 16 J. Fierro and L. G. Tejuca, *Appl. Surf. Sci.*, 1987, **27**, 453–457.
- 17 Q. Wang, Y. Peng, J. Fu, G. Z. Kyzas, S. M. R. Billah and S. An, *Appl. Catal., B*, 2015, **168–169**, 42–50.
- 18 M. M. Yung, E. M. Holmgren and U. S. Ozkan, *J. Catal.*, 2007, **247**, 356–367.
- 19 C. Resini, T. Montanari, L. Nappi, G. Bagnasco, M. Turco, G. Busca, F. Bregani, M. Notaro and G. Rocchini, *J. Catal.*, 2003, **214**, 179–190.
- 20 Q.-Y. Chen, N. Li, M.-F. Luo and J.-Q. Lu, *Appl. Catal., B*, 2012, **127**, 159–166.
- 21 C.-Y. Chen and J. J. Pignatello, *Appl. Catal., B*, 2013, **142–143**, 785–794.
- 22 M.-T. Chen, C.-F. Lien, L.-F. Liao and J.-L. Lin, *J. Phys. Chem. B*, 2003, **107**, 3837–3843.
- 23 F. Solymosi and J. Rasko, *J. Catal.*, 1995, **155**, 74–81.
- 24 Y. Wang, A.-P. Jia, M.-F. Luo and J.-Q. Lu, *Appl. Catal., B*, 2015, **165**, 477–486.
- 25 C.-C. Chuang, W.-C. Wu, M.-C. Huang, I.-C. Huang and J.-L. Lin, *J. Catal.*, 1999, **185**, 423–434.
- 26 C. Ma, D. Wang, W. Xue, B. Dou, H. Wang and Z. Hao, *Environ. Sci. Technol.*, 2011, **45**, 3628–3634.
- 27 W.-C. Wu, C.-C. Chuang and J.-L. Lin, *J. Phys. Chem. B*, 2000, **104**, 8719–8724.
- 28 C. Su, J.-C. Yeh, C.-C. Chen, J.-C. Lin and J.-L. Lin, *J. Catal.*, 2000, **194**, 45–54.
- 29 C.-W. Tang, L.-C. Hsu, S.-W. Yu, C.-B. Wang and S.-H. Chien, *Vib. Spectrosc.*, 2013, **65**, 110–115.
- 30 I. Maupin, L. Pinard, J. Mijoin and P. Magnoux, *J. Catal.*, 2012, **291**, 104–109.
- 31 S. Cao, H. Wang, F. Yu, M. Shi, S. Chen, X. Weng, Y. Liu and Z. Wu, *J. Colloid Interface Sci.*, 2016, **463**, 233–241.